CHALMERS

UNIVERSITY OF TECHNOLOGY

Tracing the atomic nitrogen abundance in star-forming regions with ammonia deuteration

(article starts on next page)

Tracing the atomic nitrogen abundance in star-forming regions with ammonia deuteration

Kenji Furuya[1]★ and Magnus V. Persson[2]

[1]*Center for Computational Sciences, University of Tsukuba, 1-1-1 Tennoudai, Tsukuba 305-8577, Japan*
[2]*Department of Space, Earth and Environment, Chalmers University of Technology, Onsala Space Observatory, SE-439 92 Onsala, Sweden*

ABSTRACT

Partitioning of elemental nitrogen in star-forming regions is not well constrained. Most nitrogen is expected to be partitioned among atomic nitrogen (N I), molecular nitrogen (N_2), and icy N-bearing molecules, such as NH_3 and N_2. N I is not directly observable in the cold gas. In this paper, we propose an indirect way to constrain the amount of N I in the cold gas of star-forming clouds, via deuteration in ammonia ice, the $[ND_2H/NH_2D]/[NH_2D/NH_3]$ ratio. Using gas–ice astrochemical simulations, we show that if atomic nitrogen remains as the primary reservoir of nitrogen during cold ice formation stages, the $[ND_2H/NH_2D]/[NH_2D/NH_3]$ ratio is close to the statistical value of 1/3 and lower than unity, whereas if atomic nitrogen is largely converted into N-bearing molecules, the ratio should be larger than unity. Observability of ammonia isotopologues in the inner hot regions around low-mass protostars, where ammonia ice has sublimated, is also discussed. We conclude that the $[ND_2H/NH_2D]/[NH_2D/NH_3]$ ratio can be quantified using a combination of Very Large Array and Atacama Large Millimeter/submillimeter Array observations with reasonable integration times, at least towards IRAS 16293−2422, where high molecular column densities are expected.

Key words: astrochemistry – stars: formation – ISM: clouds – ISM: molecules.

1 INTRODUCTION

One of the most fundamental questions in the field of astrochemistry is how heavy elements are partitioned among chemical species at each evolutionary stage during star and planet formations. Nitrogen is the fifth most abundant element with the abundance of $[N/H]_{elem} = 6 \times 10^{-5}$ in the local interstellar medium (ISM; Przybilla, Nieva & Butler 2008). The partitioning of elemental nitrogen in dense star-forming regions is not well constrained. Determining it is important for several reasons. It is a key for the understanding of differential behaviour of N-bearing species from O- and C-bearing species in the gas phase in prestellar cores and nitrogen isotope fractionation chemistry (e.g. Bergin & Tafalla 2007; Rodgers & Charnley 2008). The elemental nitrogen partitioning would also affect the formation efficiency of N-bearing complex organic molecules, as, for example, N_2 is more stable than NH_3 (e.g. Daranlot et al. 2012). Furthermore, the nitrogen partitioning in star-forming clouds may affect that in protoplanetary discs (Schwarz & Bergin 2014), which would shape the composition of planets.
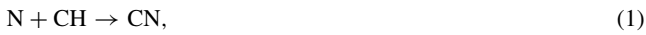
There is no clear evidence of nitrogen depletion into dust grains unlike other elements (Jenkins 2009). Then most nitrogen should be present in the gas phase in diffuse clouds. The dominant form of nitrogen in diffuse clouds is the atomic form (N I) rather than either the ionic form or molecular nitrogen (N_2) (Viala 1986; Knauth et al. 2004). In dense molecular clouds and cores, nitrogen chemistry consists of three competing processes; (i) the conversion of N I into N_2 in the gas phase, (ii) destruction of N_2 via e.g. photodissociation and reaction with He^+, and (iii) freeze out of N I and N_2 on to dust grains followed by surface reactions (e.g. Herbst & Klemperer 1973; Hidaka et al. 2011; Daranlot et al. 2012; Li et al. 2013). From these, most nitrogen is expected to be partitioned among N I, N_2, and icy N-bearing molecules, such as ammonia (NH_3) and N_2 ices. The *Spitzer* ice survey showed that the ice in star-forming regions contains, on average, ∼10 per cent of overall nitrogen as NH_3, NH_4^+, and OCN^- (Öberg et al. 2011), adopting the water ice abundance of 5×10^{-5} with respect to hydrogen nuclei (Boogert & Ehrenfreund 2004; Gibb et al. 2004; Pontoppidan, van Dishoeck & Dartois 2004). The remaining nitrogen would be present in the gas phase mainly as N I or N_2. Alternatively, there is still the possibility that a large fraction of nitrogen is locked up in N_2 ice. Indirect measurements of the upper limits on the amount of N_2 ice in molecular clouds are rather uncertain, $\lesssim 40$ per cent of overall nitrogen (Elsila, Allamandola & Sandford 1997; Boogert, Blake & Tielens 2002; Boogert, Gerakines & Whittet 2015).

Gas-phase nitrogen chemistry that converts N I into N_2 is different from oxygen and carbon chemistry, in which formation of molecules from atoms are initiated by reactions with H_3^+. It has been thought

★ E-mail: furuya@ccs.tsukuba.ac.jp

that N_2 forms via neutral–neutral reactions as follows (e.g. Herbst & Klemperer 1973; Hily-Blant et al. 2010; Daranlot et al. 2012):

$$N + CH \rightarrow CN, \tag{1}$$

$$CN + N \rightarrow N_2, \tag{2}$$

and

$$N + OH \rightarrow NO, \tag{3}$$

$$NO + N \rightarrow N_2. \tag{4}$$

According to gas-phase astrochemical models for dense clouds and cores, where the interstellar ultraviolet (UV) radiation field is significantly attenuated, either N_2 or N I can be the biggest nitrogen reservoir in steady-state, depending on the C/O elemental ratio and the elemental abundance of sulphur that are available for gas phase chemistry (Hily-Blant et al. 2010; Le Gal et al. 2014). Both the C/O ratio and the sulfur abundance would be time-dependent due to ice formation in reality. Recent gas–ice astrochemical simulations (Furuya et al. 2015; Furuya, van Dishoeck & Aikawa 2016), which trace the physical and chemical evolution from translucent clouds to denser cores, have predicted that N_2 is the primary form of nitrogen in the gas phase in cold dense cores, while most of elemental nitrogen exists as ice in the forms of NH_3 and N_2 (see also Maret, Bergin & Lada 2006; Daranlot et al. 2012).

Neither N I nor N_2 in the gas phase is directly observable in dense cores due to the cold temperatures. Several observational studies have attempted to constrain the abundance of N_2 in the gas phase via a proxy molecule, N_2H^+, which is primary formed by $N_2 + H_3^+$. Maret et al. (2006) inferred the gaseous N_2 abundance in dense cloud B68 from the observations of N_2H^+ supplemented by CO and HCO^+ observations, which were used to constrain the abundances of main destroyers for N_2H^+, i.e. CO and electrons. They concluded that the gaseous N_2 abundance is low (a few per cent) compared to overall nitrogen abundance of 6×10^{-5}, based on chemical and radiative transfer models (see also Pagani, Bourgoin & Lique 2012). The result is consistent with earlier investigation of the N_2 abundance in the gas of several cold dense clouds estimated from N_2H^+ observations with simpler analysis. McGonagle et al. (1990) estimated the gaseous N_2/CO ratio of ~ 8 per cent in dark cloud L134N, assuming that the ratio is close to the N_2H^+/HCO^+ ratio, i.e. destruction of N_2H^+ by CO is neglected. If the canonical CO abundance of 10^{-4} is adopted, the gaseous N_2 abundance is evaluated to be $\sim 8 \times 10^{-6}$ with respect to hydrogen nuclei, corresponding to ~ 30 per cent of overall nitrogen. Womack, Ziurys & Wyckoff (1992) estimated the gaseous N_2 abundance of four cold clouds to be $\sim 3 \times 10^{-6}$ with respect to hydrogen nuclei, corresponding to ~ 10 per cent of overall nitrogen.

Hily-Blant et al. (2010) suggested that the N I abundance in the gas phase can be constrained from the CN/HCN abundance ratio. The basic idea (or assumption) behind this is that both the production rate and destruction rate of CN depend on the N I abundance (see reactions 1 and 2), while for HCN, only the production rate depends on the N I abundance. Based on the observationally derived CN/HCN ratio in several prestellar cores, it was suggested that the N I abundance is low, up to a few per cent of overall nitrogen. The method, however, suffers from uncertainties of formation and destruction pathways of relevant species and their rate coefficients (Hily-Blant et al. 2010). Indeed, their astrochemical models failed

to explain the observationally derived abundances of N-bearing molecules in the pre-stellar cores.

Thus, previous studies of the nitrogen budget exploration are inconclusive, while it seems unlikely that most elemental nitrogen exists as gaseous N_2. In this paper, we propose a new way to indirectly trace the evolution of the N I abundance in the cold gas of star-forming regions via deuteration of ammonia ice. The paper is organized as follows. A proposed method is presented through a simple analytical model in Section 2, while in Section 3, the method is verified by gas–ice astrochemical simulations. Deuteration measurements of the ISM ice relies heavily on the gas observations towards inner warm (>100 K) regions in the deeply embedded protostars, where ices have sublimated. The observability of deuterated ammonia in the warm gas is discussed in Section 6. Our findings are summarized in Section 7.

2 MULTIPLE DEUTERATION OF AMMONIA ICE

Infrared ice observations have shown that ice formation (at least water ice formation) already starts before the dense core stage, where the cores gravitationally collapse to form protostars (e.g. Whittet 1993; Murakawa, Tamura & Nagata 2000). Ice formation in star-forming regions can be roughly divided into two stages (or ice mantles have two layered structure in terms of their molecular compositions; e.g. Pontoppidan 2006; Öberg et al. 2011); in the early stage, H_2O-dominated ice layers are formed. In the later stage, at higher extinction and density, the catastrophic CO freeze-out happens, and ice layers, which mainly consist of CO, and its hydrogenated species (H_2CO and CH_3OH) are formed. Observations towards deeply embedded low-mass protostars have revealed that the level of methanol deuteration, in particular the CH_3OD/CH_3OH ratio, is much higher than the HDO/H_2O ratio in the warm ($\gtrsim 100$ K) gas around the protostars, where ices have sublimated ($\sim 10^{-2}$ versus $\sim 10^{-3}$, Parise et al. 2006; Persson, Jørgensen & van Dishoeck 2013, 2014; Coutens et al. 2014). This trend indicates that deuterium fractionation is more efficient in the later stage of the ice formation when the catastrophic CO freeze-out happens (Cazaux, Caselli & Spaans 2011; Taquet, Ceccarelli & Kahane 2012; Taquet, Charnley & Sipilä 2014; Furuya et al. 2016).

It is thought that ammonia ices are primary formed via sequential hydrogenation/deuteraion of atomic nitrogen on an (icy) grain surface, supported by laboratory experiments (Hidaka et al. 2011; Fedoseev et al. 2015a; Fedoseev, Ioppolo & Linnartz 2015b). We show how the evolution of atomic nitrogen abundance during ice formation is reflected in the $[ND_2H/NH_2D]/[NH_2D/NH_3]$ ratio, using a simple analytical model. Specifically, one can distinguish two cases, whether the significant fraction of elemental nitrogen is present in the atomic form until the later stage of ice formation or not, using the $[ND_2H/NH_2D]/[NH_2D/NH_3]$ ratio. A similar analysis was made by Furuya et al. (2016) for water ice to explain the higher D_2O/HDO ratio than the HDO/H_2O ratio observed in the warm gas around a protostar ($\sim 10^{-2}$ versus $\sim 10^{-3}$; Coutens et al. 2014).

Let us consider a two-stage model (or a two-layer ice model). We denote the total amount of nitrogen locked into NH_3, NH_2D, or ND_2H ices at each stage (or in each layer) k, where $k = $ I or II, as N_k. Denoting the fraction of nitrogen locked into NX_3 ice, where X is H or D, as $P_{NX_3, k}$, one can express the amount of NX_3 ice formed in stage k as $P_{NX_3, k} N_k$. We introduce a free parameter q that satisfies $P_{ND_2H, k}/P_{NH_2D, k} = q P_{NH_2D, k}/P_{NH_3, k}$. Fedoseev et al. (2015b) found that sequential reactions of H and D atoms with atomic

nitrogen on a cold substrate lead to the $[ND_2H/NH_2D]/[NH_2D/NH_3]$ production rate ratio of $\sim 1/3$, i.e. the statistical ratio, in their experiments. On the other hand, they found that the production rates for NH_3:NH_2D:ND_2H:ND_3 (0.4:2.1:3.5:2) are deviated from the statistical distribution of 1:3:3:1, assuming the atomic D/H ratio of unity in the mixed atom beam fluxes. This result indicates that every deuteration reaction has a probability of a factor of ~ 1.7 higher to occur over the corresponding hydrogenation reactions (Fedoseev et al. 2015b). They concluded that the main reason for this deuterium enrichment is higher sticking probability of D atoms than that of H atoms in their experiments (i.e. the atomic D/H ratio on a surface is higher than unity). Indeed, the production rates obtained by their experiments can be explained by the statistical distribution with an H:D ratio of 1:1.7, i.e. NH_3:NH_2D:ND_2H:ND_3 = 0.4:2.1:3.5:2 $= 1:5.3:8.8:5 \sim 1:1.7 \times 3:(1.7)^2 \times 3:(1.7)^3 \times 1$. It should be noted that the statistical distribution of NH_3:NH_2D:ND_2H:ND_3 does depend on the atomic D/H ratio, while the statistical ratio of $[ND_2H/NH_2D]/[NH_2D/NH_3]$ does not. This characteristic makes the $[ND_2H/NH_2D]/[NH_2D/NH_3]$ ratio more useful for investigating nitrogen chemistry than the NH_3:NH_2D:ND_2H distribution (cf. Rodgers & Charnley 2002). We assume $q = 1/3$.

Using the above relations and denoting the NH_2D/NH_3 ratio and the ND_2H/NH_2D ratio as f_{D1} and f_{D2}, respectively, one can express the f_{D2}/f_{D1} ratio in the whole ice mantle as follows (cf. equation 4 in Furuya et al. 2016):

$$\frac{f_{D2}}{f_{D1}} = \frac{\sum_{k=I,II} P_{ND_2H,k} N_k \Big/ \sum_{k=I,II} P_{NH_2D,k} N_k}{\sum_{k=I,II} P_{NH_2D,k} N_k \Big/ \sum_{k=I,II} P_{NH_3,k} N_k}, \tag{5}$$

$$\approx \frac{(1+\alpha)(1+\alpha\beta^2)}{3(1+\alpha\beta)^2}, \tag{6}$$

where parameter β is defined as $P_{NH_2D,II}/P_{NH_2D,I}$, and $P_{NH_3,k}$ is assumed to be ~ 1. Parameter α is defined as $N_{N,II}/N_{N,I}$ (i.e. amount of gaseous N I in the later stages versus early stages). Then $0 < \alpha < 1$ corresponds to the case when most NH_3 ice is formed in the early stage, but the production of ammonia ice continues in the later stage with reduced efficiency. This can be interpreted that most N I is consumed by the formation of N-bearing molecules, such as N_2 and NH_3, in the early stage, and only a small amount of N I remains in the later stage. $\alpha \geq 1$ corresponds to the case when most NH_3 ice is formed in the later stage, i.e. gaseous N I (the source of NH_3 ice) remains as the primary nitrogen reservoir until the later stage, and the production of NH_3 ice is enhanced due to increased density and attenuation of UV radiation.

Fig. 1, the top panel shows the f_{D2}/f_{D1} ratio as a function of α and β. It is sufficient to consider the case of $\beta > 1$, because the deuterium fractionation becomes more efficient in the later stage. Note that to explain ~ 10 times higher D_2O/HDO ratio than the HDO/H_2O ratio, $\beta \gtrsim 100$ is required for HDO (Furuya et al. 2016). For $\alpha \lesssim 0.5$ and $\beta \gtrsim 10$, the f_{D2}/f_{D1} ratio is higher than unity and increases with decreasing α. For $\alpha \gtrsim 0.5$, the f_{D2}/f_{D1} ratio is lower than unity, regardless of β. Then the ratio allows us to prove the evolution of the N I abundance. The situation is summarized in Fig. 2.

The above discussion may be an oversimplification. For example, the gas-phase formation of ammonia followed by freeze out was
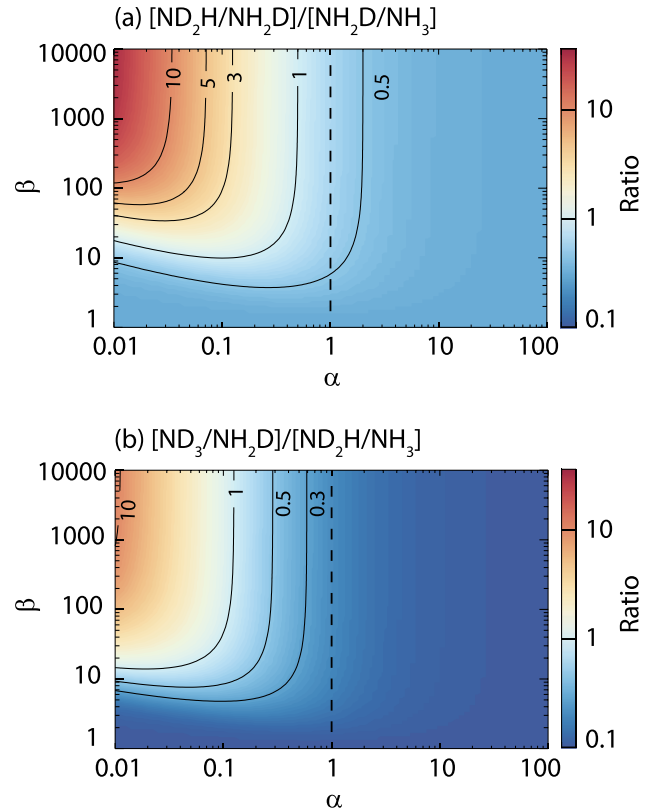

Figure 1. The $[ND_2H/NH_2D]/[NH_2D/NH_3]$ ratio (top panel) and the $[ND_3/NH_2D]/[ND_2H/NH_3]$ ratio (bottom panel) as functions of α (= N_{II}/N_I) and β (= $P_{NH_2D,II}/P_{NH_2D,I}$) in the analytical two stage model. The vertical dashed lines indicate α of unity. See the text for more information.
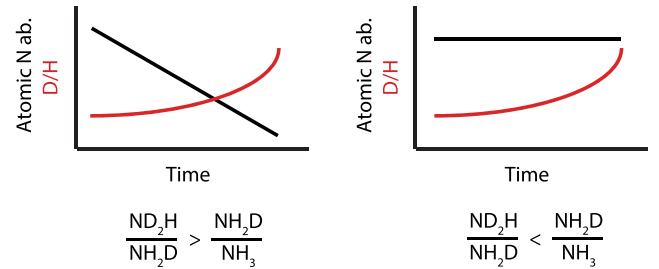

Figure 2. Left-hand panel: In the case when most of atomic nitrogen is converted into molecules during ice formation, the $[ND_2H/NH_2D]/[NH_2D/NH_3]$ ratio in the whole ice mantle is greater than unity. Right-hand panel: In the case when atomic nitrogen is the primary nitrogen reservoir during the ice formation stages, the $[ND_2H/NH_2D]/[NH_2D/NH_3]$ ratio is similar to the statistical ratio of one-thirds and lower than unity.

neglected. In the rest of this paper, the robustness of the method is tested using astrochemical simulations.

In order to find the best tracer of N I, we explored other combinations of ammonia deuteration ratios than the f_{D2}/f_{D1} ratio, using the two-stage model. Our conclusion is that the f_{D2}/f_{D1} ratio is the best. For example, the $[ND_3/NH_2D]/[ND_2H/NH_3]$ ratio shows the similar dependence on α and β (Fig. 1, bottom panel), assuming the statistical ratio, $P_{ND_3,k}/P_{ND_2H,k} = P_{ND_2H,k}/3P_{NH_2D,k}$. It is, however, required to additionally detect triply deuterated ammonia, ND_3. Then we focus on the f_{D2}/f_{D1} ratio in this paper.

3 NUMERICAL SETUP

We simulate molecular evolution from the formation of a molecular cloud to a protostellar core as in our previous studies (Furuya et al. 2015, 2016).

3.1 Physical model

We use two types of physical models: one dimensional shock model for the formation and evolution of a molecular cloud due to the compression of diffuse H I gas by supersonic accretion flows (Bergin et al. 2004; Hassel, Herbst & Bergin 2010) and one-dimensional radiation hydrodynamics simulations for the evolution of a prestellar core to form a protostar via the gravitational collapse (Masunaga & Inutsuka 2000). Here, we present brief descriptions of the two models, while more details can be found in the original papers.

The shock model simulates the physical evolution of post-shock materials, i.e. molecular cloud, considering heating and cooling processes in a plane–parallel configuration. The interstellar UV radiation field of Draine (1978) is adopted. The cosmic ray ionization rate of H_2 is set to be $1.3 \times 10^{-17}\,s^{-1}$. We assume the pre-shock H I gas density of $10\,cm^{-3}$ and the pre-shock velocity of $15\,km\,s^{-1}$ as in Furuya et al. (2015). The forming and evolving cloud has the gas density of $\sim 10^4\,cm^{-3}$ and gas and dust temperatures of ~ 10–$20\,K$, depending on time (Fig. 3, panel a). The column density of the cloud increases linearly with time, and the time it takes for the column density to reach $A_V = 1$ mag is ~ 4 Myr. In the shock model, ram pressure dominates the physical evolution rather than self-gravity.

The collapse model simulates the gravitational collapse of a prestellar core with the mass of $3.9\,M_\odot$ assuming spherical symmetry. The protostar is born at the core centre at 2.5×10^5 yr after the beginning of the collapse, corresponding to $1.4 t_{ff}$, where t_{ff} is the free-fall time of the initial central density of hydrogen nuclei $\sim 6 \times 10^4\,cm^{-3}$. After the birth of the protostar, the model further follows the physical evolution for 9.3×10^4 yr.

3.2 Chemical model

In the physical models, Lagrangian fluid parcels are traced. The kinetic rate equation is solved along the fluid parcels to obtain the molecular evolution in the fluid parcels (e.g. Aikawa 2013). The molecular abundances obtained by the cloud formation model are used as the initial abundances for the gravitational collapse model.

Our chemical model is basically the same as that used in Furuya et al. (2015). The gas–ice chemistry is described by a three-phase model, in which three distinct phases, gas-phase, icy grain surface, and the bulk of ice mantle are considered (Hasegawa & Herbst 1993). Gas-phase reactions, gas-surface interactions, and surface reactions are considered, while the bulk ice mantle is assumed to be chemically inert. We consider the top four monolayers (MLs) of the ice as a surface following Vasyunin & Herbst (2013). Our chemical network is originally based on that of Garrod & Herbst (2006), while gaseous nitrogen chemistry has been updated following recent references (Wakelam et al. 2013; Loison, Wakelam & Hickson 2014; Roueff, Loison & Hickson 2015). The network has been extended to include up to triply deuterated species and nuclear spin states of H_2, H_3^+, and their isotopologues. The state-to-state reaction rate coefficients for the H_2–H_3^+ system are taken from Hugo, Asvany & Schlemmer (2009). The self-shielding of H_2, HD, CO, and N_2 against photodissociation is taken into account (e.g. Visser, van Dishoeck & Black 2009; Li et al. 2013). The photodesorption yield per incident FUV photon is $\sim 3 \times 10^{-4}$ for water ice (Arasa

et al. 2015). We assume the yield of 10^{-3} for ammonia ice. The photodesorption yields for CO and N_2 ices are treated in a special way and given as increasing functions of the surface coverage of CO (Furuya et al. 2015). The yield for CO ice varies from 3×10^{-4} to 10^{-2}, while that for N_2 ice varies from 3×10^{-3} to 8×10^{-3} (Fayolle et al. 2011; Bertin et al. 2012, 2013).

There are some updates from the model in Furuya et al. (2015); (i) the treatment of charge exchange and proton/deuteron transfer reactions, (ii) the binding energy on a grain surface, and (ii) mass for calculating transmission probabilities of tunnelling reactions on grain surfaces. In our previous work, complete scrambling of protons and deuteron was assumed for all types of reactions (Aikawa et al. 2012). The assumption on the complete scrambling is not appropriate, at least, for charge exchange and proton/deuteron transfer reactions (Rodgers & Millar 1996; Sipilä, Caselli & Harju 2013). We relax the assumption for these two types of reactions, following Sipilä et al. (2013). This modification reduces the production rates of multiply deuterated species, such as ND_2H and ND_3, via gas-phase reactions when deuterium fractionation proceeds significantly and multiply deuterated H_3^+ becomes abundant.

Laboratory experiments have shown that the binding energy of species depends on the type of surfaces (e.g. Fayolle et al. 2016). As described in Section 2, the surface composition of the ISM ice can vary from an H_2O-rich polar surface to a CO-rich apolar surface, depending on time. In our model, the binding energy of species i, $E_{des}(i)$, is calculated as a function of surface coverage of species j, θ_j, where $j = H_2$, CO, CO_2, or CH_3OH:

$$E_{des}(i) = (1 - \Sigma_j \theta_j) E_{des}^{H_2O}(i) + \Sigma_j \theta_j E_{des}^j(i), \tag{7}$$

where $E_{des}^j(i)$ is the binding energy of species i on species j. The set of the binding energies on a water ice substrate, $E_{des}^{H_2O}$, is taken from Collings et al. (2004)Garrod & Herbst (2006), and Wakelam et al. (2017). In particular for this work, $E_{des}^{H_2O}$ for O I, N I, CO, and N_2 is set to be 1320, 720, 1300, and 1170 K, respectively, following laboratory experiments (Fayolle et al. 2016; Minissale, Congiu & Dulieu 2016). $E_{des}^{H_2O}$ for atomic hydrogen and H_2 is set to be 550 K. There is no laboratory data or estimate for most $E_{des}^j(i)$ in the literature. In order to deduce E_{des}^j for all species, where j is either H_2, CO, CO_2, or CH_3OH, we assume scaling relations (cf. Taquet et al. 2014)

$$E_{des}^j(i) = \epsilon_j E_{des}^{H_2O}(i), \tag{8}$$

where ϵ_j is $E_{des}^j(j)/E_{des}^{H_2O}(j)$. We adopt $\epsilon_{H_2} = 23/550$, $\epsilon_{CO} = 855/1300$, $\epsilon_{CO_2} = 2300/2690$, and $\epsilon_{CH_3OH} = 4200/5500$ (e.g. Öberg et al. 2005; Cuppen & Herbst 2007; Noble et al. 2012). Fayolle et al. (2016) found that the binding energy ratio of N_2 to CO is around 0.9 regardless of a type of a substrate in their laboratory experiments. This partly supports the above assumption that ϵ_j is independent of adsorbed species i. The energy barrier against surface diffusion by thermal hopping is set to be $0.45 E_{des}$ for all species.

The sticking probability of neutral species i on a grain surface is given as a function of the binding energy and dust temperature:

$$S(i) = (1 - \Sigma_j \theta_j) S'(T_{dust}, E_{des}^{H_2O}(i)) + \Sigma_j \theta_j S'(T_{dust}, E_{des}^j(i)), \tag{9}$$

where S' is the sticking probability formula recommended by (He, Acharyya & Vidali 2016, see their equation 1), who experimentally investigated the sticking probability for stable molecules on non-porous amorphous water ice. Equation (9) gives, in general, the sticking probability of around unity for all species at ~ 10 K, while the probability is close to zero well above the sublimation temperature of each species.
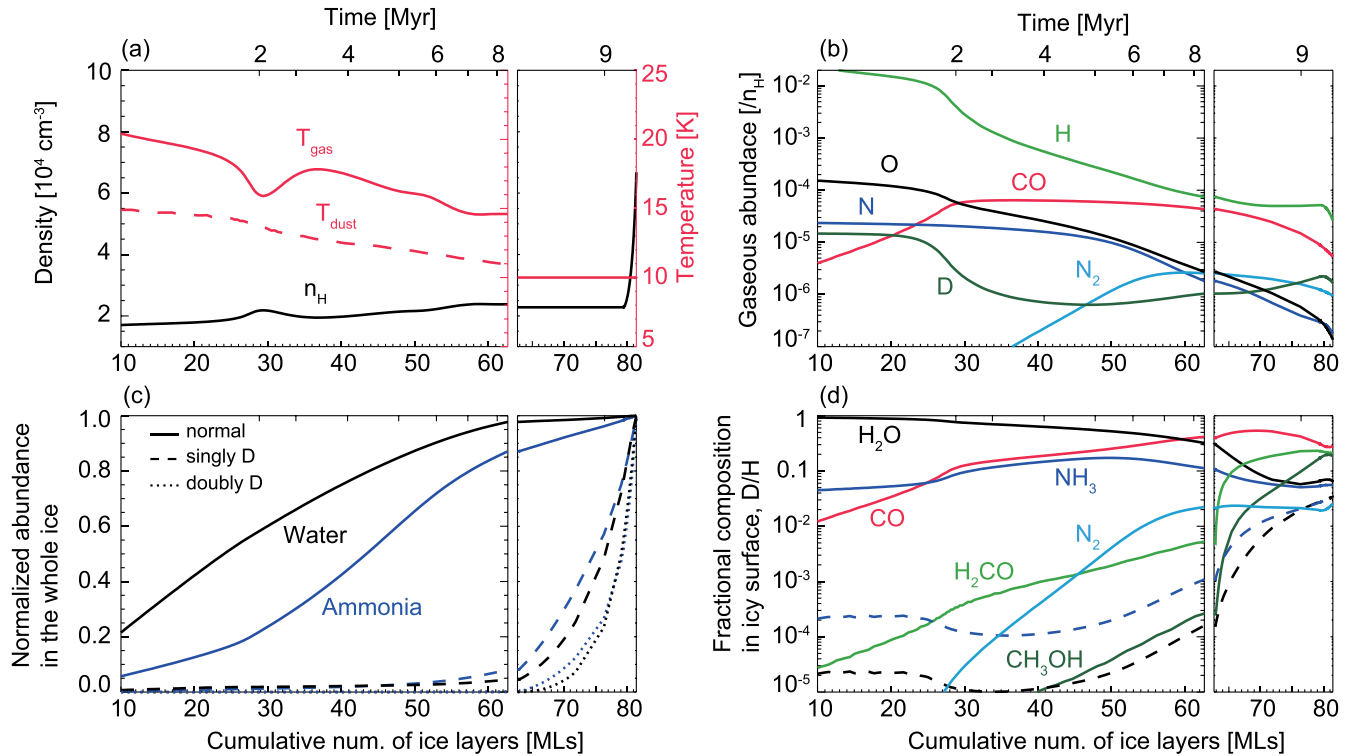
Figure 3. (a) Physical parameters, (b) abundances of selected gaseous species with respect to hydrogen nuclei, and (d) fractional composition in the surface ice layers as functions of the cumulative number of ice layers. The dashed lines in panel (d) indicate the HDO/H$_2$O ratio (black) and the NH$_2$D/NH$_3$ ratio (blue). As the total number of ice layers increases with time during the cold ice formation stages, the horizontal axis can be read as time (see the label at the top). In each panel, $\lesssim$60 MLs correspond to the formation stage of a molecular cloud, and $\gtrsim$60 MLs corresponds to the 1 Myr static core phase and the early collapse phase (2.6×10^5 yr after the onset of collapse), where dust temperature is 10 K. The results are shown for the fluid parcel, which reaches 5 au from the central star at the final time of the simulation. Panel (c) shows the abundances of non-deuterated and deuterated forms of water ice (black) and ammonia ice (blue) normalized by their maximum abundances. Note that the visual extinction for calculating photochemical rates increases from 2 mag at the end of the cloud formation stage to >5 mag at the core stage.

Grain-surface reactions are assumed to occur by the Langmuir–Hinshelwood mechanism. When the rates of surface reactions with activation energy barriers are calculated, reaction-diffusion competition is considered (e.g. Chang, Cuppen & Herbst 2007; Garrod & Pauly 2011). The activation energy barriers are assumed to be overcome either thermally or via quantum tunnelling, whichever is faster. The transmission probability of tunnelling reactions is calculated assuming a rectangular potential barrier, using the reduced mass of the system (Tielens & Hagen 1982). As pointed out by several authors, the use of the reduced mass of the system for hydrogen abstraction reactions, such as OH + H$_2$ → H$_2$O + H, underestimates the transmission probability by orders of magnitude (Hidaka et al. 2009; Oba et al. 2012; Lamberts et al. 2014). We use the mass of a hydrogen (deuterium) atom instead of the reduced mass in the calculation of the transmission probability of hydrogen (deuterium) abstraction reactions.

3.3 Parameters

Elemental abundances adopted in this work are the so called low metal abundances and taken from Aikawa & Herbst (1999). The elemental abundances relative to H are 7.9×10^{-5} for C, 2.5×10^{-5} for N, and 1.8×10^{-4} for O. Deuterium abundance is set to be 1.5×10^{-5} (Linsky 2003). Our model also includes He, S, Si, Fe, Na, Mg, P, and Cl. All the elements, including H and D, are initially assumed to be in the form of either neutral atoms or atomic

ions, depending on their ionization potential. Then the ortho-to-para ratio of H$_2$ is calculated explicitly in our model without making an arbitrary assumption on its initial value. For initial molecular abundances of the collapse model, we use the molecular abundances at the epoch when the column density reaches 2 mag in the cloud formation model.

Before the onset of the core collapse, we assume that the prestellar core keeps its hydrostatic structure for 10^6 yr ($\sim$5.6$t_{\rm ff}$). The visual extinction at the outer edge of the core is set to be 5 mag, being irradiated by the interstellar radiation field of Draine (1978). The cosmic ray ionization rate of H$_2$ is set to be 1.3×10^{-17} s^{-1} throughout the simulations, while the flux of FUV photons induced by cosmic-rays is set to be 3×10^3 cm^{-2} s^{-1}.

4 SIMULATION RESULTS

4.1 Ice chemistry

Fig. 3 shows abundances of selected gaseous species with respect to hydrogen nuclei (panel b) and the fractional composition in the surface ice layers (panel d) as functions of the cumulative number of layers formed in the ice mantle. In each panel, $\lesssim$60 MLs correspond to the cloud formation stage, while $\gtrsim$60 MLs correspond to the core stage. For the core stage, the results for the fluid parcel that reaches 5 au from the central star at the final simulation time are shown. The label at the top represents time, in which $t = 0$ corresponds to the

time when the fluid parcel passes through the shock front, i.e. the onset of cloud formation.

H_2O ice is the dominant component of the lower ice mantles ($\lesssim 60$ MLs) formed in the early times, while the upper ice layers ($\gtrsim 60$ MLs) mainly consists of CO and its hydrogenated species, H_2CO and CH_3OH. The significant freeze out of CO happens later than the formation of most of water ice in our model, because the freeze out of CO is a self-limited process (Furuya et al. 2015); with increasing the CO coverage on a surface, the photodesorption yield of CO is enhanced and the binding energy of CO is reduced, the latter of which enhances the non-thermal desorption rate due to the stochastic heating by cosmic rays. The conversion of CO ice to CH_3OH ice becomes more efficient with increasing the abundance ratio of H atoms to CO in the gas phase ($\gtrsim 70$ MLs; e.g. Charnley, Tielens & Rodgers 1997). The HDO/H_2O ratio and the NH_2D/NH_3 ratio are much higher in the upper ice mantles than those in the lower ice mantles, due to the CO freeze-out, the drop of the ortho-to-para ratio of H_2, and the attenuation of UV radiation field (Furuya et al. 2016).

4.2 Elemental nitrogen partitioning

At the end of ice formation, when the number of ice layers reaches ~ 80 MLs, most elemental nitrogen is distributed among NH_3 ice (76 per cent), gaseous and icy N_2 (22 per cent), and N I (<1 per cent). In our model, NH_3 ice forms via sequential surface reactions,

$$N + H \rightarrow NH, \tag{10}$$

$$NH + H \rightarrow NH_2, \tag{11}$$

$$NH_2 + H_2 \rightarrow NH_3 + H. \tag{12}$$

The last reaction has an activation energy barrier of 2700 K in the gas phase (Espinosa-Garcia & Corchado 2010; Hidaka et al. 2011), and the transmission probability of this barrier-mediate reaction is set to be $\sim 10^{-9}$. Note that reaction-diffusion competition is considered in our model. In our surface chemical network, the barrierless reaction $NH_2 + H \rightarrow NH_3$ is included, in addition to reaction (12). Nevertheless, reaction (12) is more efficient in our model, because the adsorption rate of H_2 on grain surfaces is much higher than that of atomic H, and thus H_2 is much more abundant than atomic H on surfaces. The rate-limiting step of the NH_3 ice formation is the adsorption of N I on a surface, and thus the formation rate of NH_3 ice should not depend on the surface reaction rates significantly. The NH_3 ice formation is balanced with the photodesorption of NH_3 ice in the cloud formation stage, and then the time-scale of NH_3 ice formation is much longer than the freeze out time-scale of N I ($\sim 10^5$ yr for the density of 10^4 cm^{-3}). In the core stage, the interstellar UV radiation is attenuated significantly, and the time-scale of NH_3 ice formation is determined by the freeze out of N I.

Interestingly, the formation of NH_3 ice helps the conversion of N I into N_2 in the gas phase through photodesorption; photodesorbed NH_3 is further photodissociated in the gas phase, and the photofragment (NH_2 or NH; Heays, Bosman & van Dishoeck 2017) reacts with N I to form N_2. NH and NH_2 also react with C-bearing species to form CN, eventually leading to N_2 formation by reaction (2). Fig. 4 shows the impact of NH_3 photodesorption on the conversion of N I into N_2. The solid lines represent our fiducial model, while the dashed lines represent the model, in which the products of NH_3 photodesorption are set to be N + 3H. The comparison between
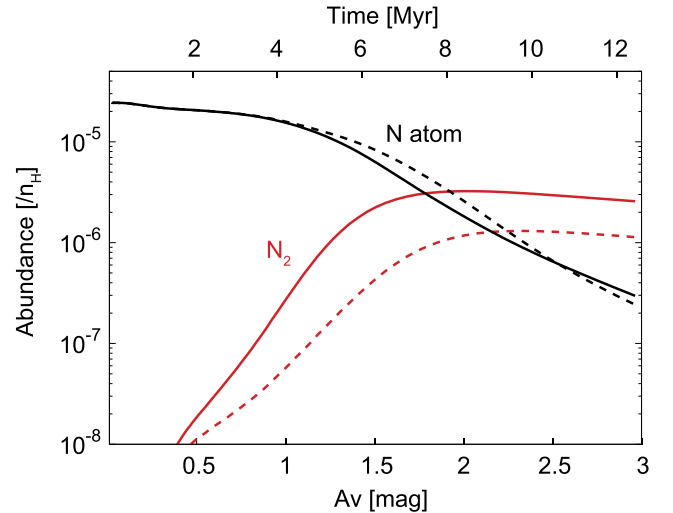

Figure 4. Abundances of atomic nitrogen and N_2 in the cloud formation model. For N_2, the total abundance (gas and ice are combined) is shown. Solid lines represent our fiducial model in which the product of NH_3 photodesorption is set to be NH_3, while dashed lines represent the model in which the products of NH_3 photodesorption are set to be N + 3H. For this figure, the models of the cloud formation were run until the column density of the cloud reaches 3 mag.

the two models indicates that the formation of nitrogen hydrides in the gas phase triggered by NH_3 photodesorption accelerates the conversion of N I into N_2. Note that in the context of dark cloud chemistry where interstellar UV radiation field is neglected, NH and NH_2 are produced from N_2 via ion-neutral gas-phase chemistry (e.g. Hily-Blant et al. 2010).

N_2 ice is formed via the adsorption of gaseous N_2. Reaction between N_2 and atomic hydrogen is significantly endothermic, $>10^4$ K (Hidaka et al. 2011, and references therein), and thus N_2 ice does not react with icy H atoms.

4.3 Ammonia deuteration

Fig. 5 shows the radial profiles of the abundances of selected species with respect to hydrogen nuclei (top panel) and the deuterium fractionation ratios in water and ammonia (bottom panel) in the protostellar envelope. Both icy water and ammonia sublimate into the gas phase at $R \lesssim 100$ au at temperatures of $\gtrsim 150$ K in our model. N_2 trapped in the ice mantle also sublimates into the gas phase with the sublimation of water and ammonia ices.

The deuteration ratios of ammonia and water in the gas phase of the protostellar envelope have two common characteristics in our model, both of which have been observationally confirmed for water (Coutens et al. 2012, 2014; Persson et al. 2013). First, the abundance ratio between singlydeuterated and non-deuterated forms in the inner warm regions ($T \gtrsim 150$ K) is smaller than that in the outer cold envelope (e.g. 4×10^{-3} versus 0.2 for ammonia in our model). The deuteration ratio in the outer envelope is determined by the gas-phase ion-neutral chemistry, while that in the warm regions is dominated by ice sublimation (see also Aikawa et al. 2012; Taquet et al. 2014). Secondly, in the warm regions, the abundance ratio between doubly deuterated and singly deuterated forms is higher than that between singly deuterated and non-deuterated forms (e.g. $[ND_2H/NH_2D]/[NH_2D/NH_3] \sim 4$). This is consistent with our prediction from the analytical two-stage model; in the case when most of atomic nitrogen is consumed during ice
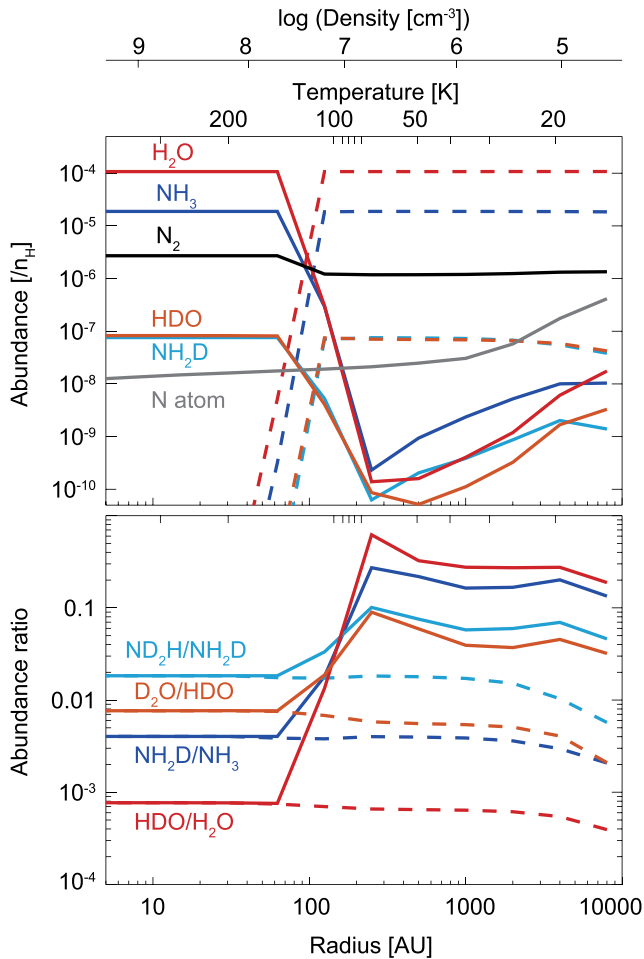
Figure 5. Abundances of selected species with respect to hydrogen nuclei (top) and the abundance ratios (bottom) in the protostellar envelope in the fiducial model at 9.3×10^4 yr after the protostellar birth. The labels at the top represents the temperature and density structures. The solid lines represent gaseous species, while the dashed lines represent species in the whole ice mantle.

formation stages, the [ND$_2$H/NH$_2$D]/[NH$_2$D/NH$_3$] ratio in the whole ice mantle is greater than unity. The [D$_2$O/HDO]/[HDO/H$_2$O] ratio in the inner warm regions is 10 in our model, which is consistent with our previous work (Furuya et al. 2016). The molecular abundances and the deuterium fractionation ratios in the warm regions are summarized in Table 1.

Fig. 3 panel (c) shows the abundances of non-deuterated and deuterated forms of water ice (black) and ammonia ice (blue) normalized by their maximum abundances. The formation of NH$_3$ ice is

behind that of H$_2$O ice (in terms of the analytical two-stage model, α for nitrogen is smaller than that for oxygen), while the timing of the formation of deuterated ammonia ice and deuteratd water ice is similar. These are reflected in the lower [ND$_2$H/NH$_2$D]/[NH$_2$D/NH$_3$] ratio than the [D$_2$O/HDO]/[HDO/H$_2$O] ratio in the warm regions in our fiducial model. Also the delayed NH$_3$ ice formation is reflected in the NH$_2$D/NH$_3$ ratio in our fiducial model; the NH$_2$D/NH$_3$ ratio is between the HDO/H$_2$O ratio and the CH$_3$OD/CH$_3$OH ratio (but see Section 5.2).

5 PARAMETER DEPENDENCES

5.1 Primary nitrogen reservoir

In our fiducial model, most nitrogen is locked in NH$_3$ ice (76 per cent of overall nitrogen and the NH$_3$/H$_2$O abundance ratio of ~18 per cent), as widely seen in published gas–ice astrochemical models (e.g. Chang & Herbst 2014; Pauly & Garrod 2016). In this subsection, we discuss the effect of the primary nitrogen reservoir on the [ND$_2$H/NH$_2$D]/[NH$_2$D/NH$_3$] ratio.

As discussed in Section 4.2, photodesorption of NH$_3$ assists the conversion of N I into N$_2$, while it slows down the accumulation of NH$_3$ ice. Then it is expected that the fraction of nitrogen locked in NH$_3$ ice decreases with increasing the photodesorption yield of NH$_3$, while that of N$_2$ increases. The recently measured photodesorption yield for pure NH$_3$ ice in laboratory is $2.1^{+2.1}_{-1.0} \times 10^{-3}$ per incident photon (Martin-Domenech, Cruz-Diaz & Munoz Caro 2017). We run the model in which the photodesorption yield of NH$_3$ is 3×10^{-3} (i.e. three times larger than in our fiducial model). Hereafter, we refer to this model as model B. Fig. 6 compares the fractions of elemental nitrogen locked in the selected species in our fiducial model (panel a) and those in model B (panel b). The horizontal axis is the cumulative number of layers formed in the ice mantle normalized by the total number of ice layers at the end of ice formation (70–80 MLs depending on a model). As has been expected, the fraction of elemental nitrogen locked in N$_2$ is higher in model B than in the fiducial model (51 per cent versus 22 per cent). In model B, NH$_3$ ice, gas and icy N$_2$, and N I contain 46 per cent, 51 per cent, and 0.1 per cent of overall nitrogen, respectively. Partitioning of nitrogen between NH$_3$ ice and N$_2$ is sensitive to the photodesorption yield of NH$_3$ ice.

Both in the fiducial model and in model B, most nitrogen is locked in molecules. The analytical model presented in Section 2 predicts that the [ND$_2$H/NH$_2$D]/[NH$_2$D/NH$_3$] ratio is similar to the statistical value of 1/3 and lower than unity when N I remains as the primary nitrogen reservoir. In order to simulate this case, we run an additional model (labelled model C). In model C, the rates of any reactions that include N I as a reactant are reduced by a factor of 20. Then in model C, the formation of both NH$_3$ ice and

Table 1. Summary of model results.

Model[a]	N I (per cent)[b]	N$_2$ (per cent)[b]	NH$_3$ (per cent)[b]	$\frac{NH_3}{H_2O}$	$\frac{NH_2D}{NH_3}$	$\frac{ND_2H}{NH_2D}$	$\frac{ND_2H/NH_2D}{NH_2D/NH_3}$	$\frac{HDO}{H_2O}$	$\frac{D_2O/HDO}{HDO/H_2O}$	$\frac{CH_3OD}{CH_3OH}$
A[c]	5.1(−2)	22	76	1.8(−1)	4.0(−3)	1.8(−2)	4.6	7.7(−4)	10	1.4(−2)
B	0.1	51	46	1.1(−1)	1.0(−2)	1.8(−2)	1.8	7.6(−4)	9.5	1.3(−2)
C	57	13	28	6.5(−2)	2.0(−2)	1.3(−2)	6.6(−1)	7.9(−4)	8.3	1.3(−2)
A'[d]	6.4(−2)	29	69	1.6(−1)	9.6(−3)	1.8(−2)	1.9	7.9(−4)	9.4	1.4(−2)

[a] Values in the warm gas ($T > 150$ K) at 9.3×10^4 yr after the protostellar birth. $a(− b)$ means $a \times 10^{−b}$.

[b] Fractions of elemental nitrogen in percentage form.

[c] Our fiducial model.

[d] Similar to model A, but without reaction (12) and the same reactions of the corresponding deuterium isotopologues.
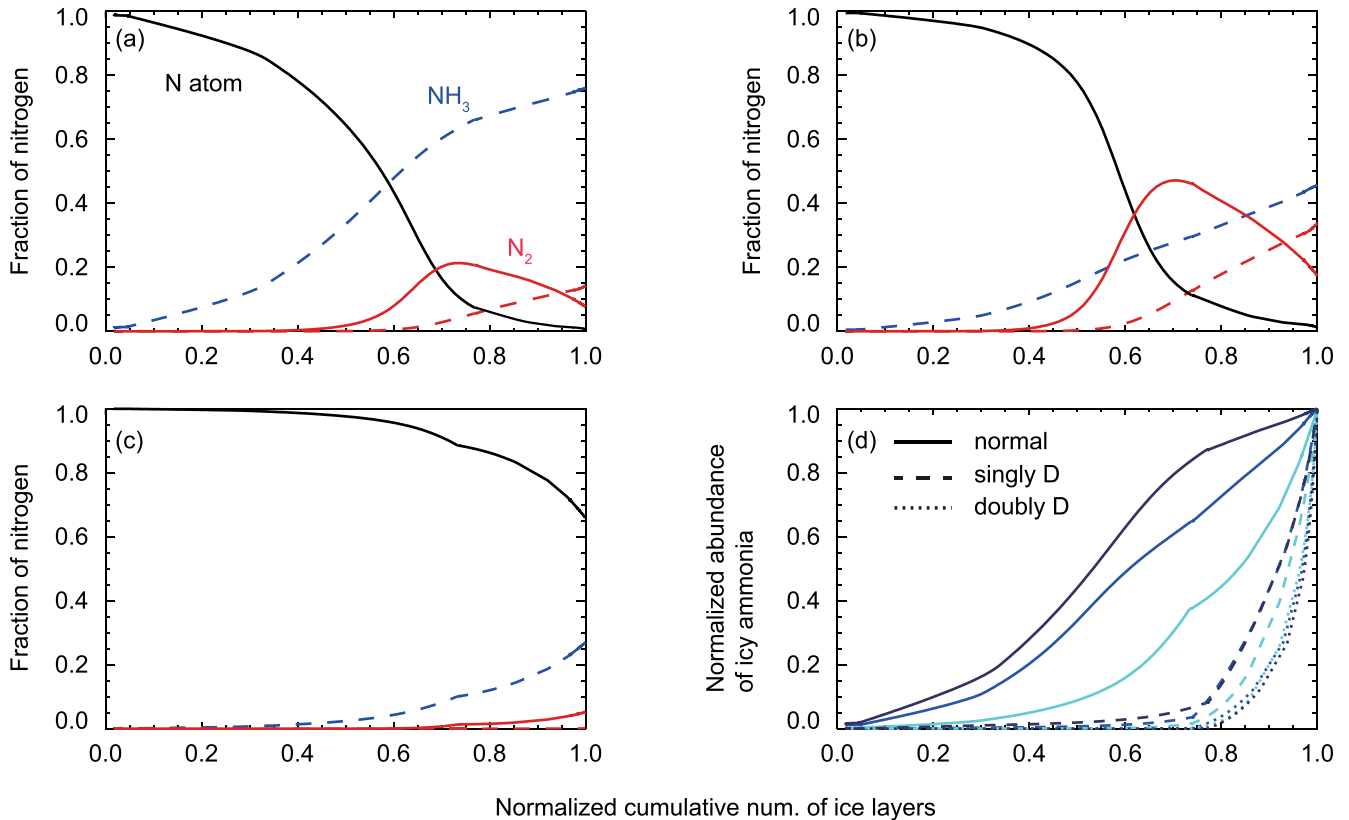
Figure 6. Fraction of elemental nitrogen in N I, N_2, and NH_3 in the fiducial model (panel a), model B (panel b), and model C (panel c) in the same fluid parcel shown in Fig. 3 as functions of the cumulative number of ice layers normalized by the maximum number of ice layers. The solid lines represent gaseous species, while the dashed lines represent icy species. Panel (d) shows abundances of non-deuterated and deuterated forms of ammonia ice normalized by their maximum abundances in the fiducial model (navy), model B (blue), and model C (cyan). Note that the maximum number of ice layers and the maximum abundances of ammonia ices are different among the models.

N_2 gas is slowed down compared to that in the fiducial model. This assumption is very artificial and model C should be considered as just a numerical experiment. In model C, NH_3 ice, gas and icy N_2, and N I contain 28 per cent, 13 per cent, and 57 per cent of overall nitrogen, respectively (Table 1 and Fig. 6, panel c).

The $[ND_2H/NH_2D]/[NH_2D/NH_3]$ ratio is the largest in the fiducial model (4.6) followed in order by model B (1.8) and model C (0.66). The conversion of N I into NH_3 ice and N_2 occurs earlier in the fiducial model than in model B, and the significant fraction of nitrogen remains as N I even at the end of the ice formation stage in model C (Fig. 6, panels a,b,c). Thus, as predicted by the analytical stage model, the evolution of the N I abundance is reflected in the $[ND_2H/NH_2D]/[NH_2D/NH_3]$ ratio. Fig. 6 panel d shows when non-deuterated and deuterated forms of ammonia ice are mainly formed in the fiducial model, in model B, and in model C. The fraction of ammonia ice without significant deuterium fractionation ($\lesssim 0.8$ in the normalized cumulative number of ice layers) is the largest in the fiducial model and the smallest in model C (in terms of the analytical two-stage model, α is the smallest in the fiducial model and the largest in model C).

5.2 Additional considerations

In our fiducial model, the main formation reaction of NH_3 ice is the barrier-mediated reaction $NH_2 + H_2 \rightarrow NH_3 + H$ on a grain surface rather than the barrierless reaction $NH_2 + H \rightarrow NH_3$. Furuya et al. (2015) found that the level of water ice deuteration depends

on which formation reaction, the barrier-mediated reaction $OH + H_2 \rightarrow H_2O + H$ or the barrierless reaction $OH + H \rightarrow H_2O$ is more effective. When the barrier-mediated reaction is the primary formation reaction, water ice deuteration can be significantly suppressed through the cycle of photodissociation by interstellar UV radiation and reformation of water ice, which efficiently removes deuterium from water ice chemistry (see also Kalvāns et al. 2017). We confirmed that the same mechanism is at work for ammonia as well as water. In our fiducial model, the NH_2D/NH_3 ratio in the icy species ($\sim 10^{-4}$–10^{-3}) is smaller than the atomic D/H ratio in the gas phase ($\sim 10^{-3}$–10^{-2}) in the cloud formation stage by a factor of $\gtrsim 10$, while the difference becomes much smaller in the core stage (Fig. 3 panels b, d). While laboratory experiments demonstrated that $OH + H_2 \rightarrow H_2O + H$ proceeds on a cold surface by quantum tunnelling (Oba et al. 2012), to the best of our knowledge, $NH_2 + H_2 \rightarrow NH_3 + H$ on a cold surface has not been studied in laboratory.

In order to check the dependence of our results on the main formation reaction of NH_3 ice, we rerun our fiducial model without the surface reaction $NH_2 + H_2$ and the same reactions of the corresponding deuterium isotopologues. Compared to the fiducial model, the NH_2D/NH_3 ratio in the warm gas ($T \gtrsim 150\,K$) is enhanced by a factor of ~ 2, and close to the CH_3OD/CH_3OH ratio. The $[ND_2H/NH_2D]/[NH_2D/NH_3]$ ratio is reduced by a factor of ~ 2, but still much higher than that in model C, in which N I remains as the primary reservoir of nitrogen. The main formation reaction of NH_3 ice does not affect our results qualitatively.

Fedoseev et al. (2015a) performed laboratory experiments for ammonia ice formation in CO ice through sequential hydrogenation of N atoms. They found that HNCO forms in their experiments likely via the reaction,

$$NH + CO \rightarrow HNCO, \tag{13}$$

where NH is the intermediate in the formation of NH_3. Similarly, formamide (NH_2CHO) may be formed via the following surface reaction (Fedoseev et al. 2016):

$$NH_2 + H_2CO \rightarrow NH_2CHO + H. \tag{14}$$
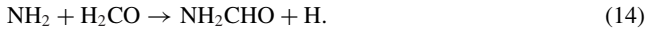
These two reactions, which are not included in our surface chemical network, may reduce the production rate of ammonia ice on CO-rich layers and thus could enhance the $[ND_2H/NH_2D]/[NH_2D/NH_3]$ ratio.

Recent observations of the warm gas around low-mass protostar IRAS 16293−2422B (Coutens et al. 2016) found that the levels of deuteration in HNCO and NH_2CHO are similar to the CH_3OD/CH_3OH ratio. This finding is consistent with the scenario that HNCO and NH_2CHO are formed via surface reactions on CO-rich ice layers (Coutens et al. 2016). The observed HNCO and NH_2CHO column densities are, however, lower than the CH_3OH column density in the same source by factors of ∼1000 (Coutens et al. 2016; Jørgensen et al. 2016). According to infrared ice observations, the NH_3/CH_3OH ratio in the cold outer envelope of low-mass protostars is of the order of unity (Öberg et al. 2011). These indicate that either atomic nitrogen is already poor when the catastrophic CO freeze-out happens or only the small fraction of atomic nitrogen adsorbed on grain surfaces contributes to the formation of HNCO and NH_2CHO ices. In either case, reactions (13) and (14) would not affect our results qualitatively.

6 DISCUSSION: OBSERVABILITY OF DEUTERATED AMMONIA IN THE WARM GAS

There have been several observational studies to quantify the ammonia deuteration in star formation regions. Most measurements are of the cold gas in prestellar cores and in outer envelopes of deeply embedded protostars, using single dish telescopes (e.g. Lis et al. 2002; Roueff et al. 2005; Harju et al. 2017). For example, observations towards the prestellar core I16293E show ratios of $NH_2D/NH_3 \approx ND_2H/NH_2D \approx 20$ per cent (Loinard et al. 2001; Roueff et al. 2005). Measurements for the cold-large-scale envelope towards a deeply embedded low-mass protostar NGC 1333–IRAS 4A show an NH_2D/NH_3 ratio of ∼7 per cent (Shah & Wootten 2001). These extremely high NH_2D/NH_3 and ND_2H/NH_2D ratios are reasonably well reproduced in the outer cold regions of our protostellar envelope model ($\gtrsim 1000$ au, Fig. 5).

While in agreement with the modelling presented here, these previous measurements, however, would not reflect the deuteration in ice, being supported by astrochemical models (Fig. 5, see also Aikawa et al. 2012; Taquet et al. 2014). The nitrogen deuterium fractionation in the cold gas in the large-scale envelope do not differ significantly between the various models. The ratio deduced in the large-scale envelope is thus not a suitable indicator for distinguishing between the different scenarios of atomic nitrogen evolution. To measure the ammonia deuteration in the bulk ice, interferometric observations towards the recently sublimated warm gas in the inner regions of protostars are necessary. It has been already shown that the values of water deuteration measured in the large-scale cold envelope are much higher than that measured in the warm envelope

around protostars, where water ice has sublimated (Coutens et al. 2012; Persson et al. 2013).

To assess the possibility of distinguishing between the different models with observations, we here calculate the spectra of NH_3, NH_2D, and ND_2H towards a typical Class 0 protostar assuming the ratios in model A in Table 1. The synthetic spectra are compared to typical sensitivities in the relevant Karl G Jansky Very Large Array (VLA) and Atacama Large Millimeter/submillimeter Array (ALMA) bands with reasonable integration times (10 h with VLA and 4 h with ALMA) calculated using officially available tools (sensitivity calculators[1]) at a target resolution of 0.4 arcsec. This can then aid the planning of future observations.

To this date, very few detections of compact ammonia emission towards a deeply embedded protostar exists. Choi et al. (2007) and Choi, Tatematsu & Kang (2010) presented detections of the $2_{2,0a} - 2_{2,0s}$ and $3_{3,0a} - 3_{-3,0s}$ transitions of NH_3 using the VLA telescope at high resolution (∼0.3 arcsec) towards the protobinary source IRAS 4A, located at a distance of 235 pc (Hirota et al. 2008). In Fig. 5, the relevant volume hydrogen density in the warm region is typically $>10^8$ cm^{-3}, which is well above the critical density for all NH_3 lines (e.g. Maret et al. 2009), which shows that LTE is prevalent in these sources and scales. We can then use general relations, for example, Goldsmith & Langer (1999), to reproduce the observed line fluxes. A similar method to constrain an abundance is presented in, for example Persson et al. (2013) and Coutens et al. (2016). The detected ammonia spectral lines are well reproduced by a column density of 6–7 × 10^{17} cm^{-2} at an excitation temperature of 250–300 K, assuming LTE and accounting for the optical depth. For Class I sources, Sewilo et al. (2017) presented archival observations of ammonia towards the source HH111/HH121 at medium spatial resolution (∼8 arcsec). The sparse results on compact ammonia emission highlight even further the importance of more observations constraining the ammonia abundances in these warm inner regions of deeply embedded protostars.

With observations of $H_2^{18}O$ (Persson et al. 2013, 2014), we can estimate the NH_3/H_2O column density ratio in the warm gas,[2] which can be compared with that obtained by infrared ice observations. For the north-western source of the IRAS 4A binary, the H_2O column density was constrained by Persson et al. (2014) to 4.4 × 10^{18} cm^{-2}, and we get an NH_3/H_2O column density ratio in the warm gas of 13–16 per cent. This value is close to the NH_3/H_2O ice column density ratio in low-mass protostellar envelopes, 3–10 per cent, depending on sources (Boogert et al. 2015, and references therein), indicating that our LTE method is reasonable. Note that IRAS 4A is a highly extincted Class 0 source and ice measurements are not available.

To estimate the line fluxes of NH_3, NH_2D, and ND_2H, we will use the deeply embedded source IRAS 16293−2422 (hereafter I16293). It is located in the ρ Ophiucus star-forming complex, at a distance of 120 pc (Loinard et al. 2008), and is a binary source with a 5 arcsec (600 au) separation, where the north western source is referred to as A and the south easter source is referred to as B. The molecular content of I16293 has been extremely well explored with both interferometers and single dish telescopes (Bottinelli et al. 2004; Bisschop et al. 2008; Jørgensen et al. 2011). Jørgensen et al. (2016) presents an extensive review of the work done towards I16293.

---

[1] VLA https://obs.vla.nrao.edu/ect/, ALMA https://almascience.eso.org/proposing/sensitivity-calculator

[2] Assuming a $^{16}O/^{18}O$ ratio of 560 (relevant for these galactocentric distances Wilson & Rood 1994; Wilson 1999)

The water isotopologue $H_2^{18}O$ was observed at high resolution with ALMA and SMA (Persson et al. 2013), and it was only possible to deduce the column density towards source A. Using the derived water column density and the NX_3/H_2O abundance ratio in our models (X is H or D; Table 1), we can estimate the NX_3 column density in I16293. Assuming the conservative scenario of model A from Table 1, we here estimate the column densities of NH_3, NH_2D, and ND_2H. The H_2O water column density from Persson et al. (2013) is $5.3 \times 10^{20}\,cm^{-2}$. Assuming an excitation temperature of 200 K towards the warm gas of I16293 as in the innermost regions of the model (cf. Fig. 5), similar to, for example, Persson et al. (2013), we can calculate the expected line strengths. The water column density gives a column density of $9.5 \times 10^{19}\,cm^{-2}$ for NH_3, $3.8 \times 10^{17}\,cm^{-2}$ for NH_2D, and $6.9 \times 10^{15}\,cm^{-2}$ for ND_2H. For the modelled spectra, we assume a size of the emitting region of 0.4 arcsec and a beam size of 0.4 arcsec.

The $NH_3v{=}0$ transition frequencies and constants are taken from the Spectral Line Atlas of Interstellar Molecules, available at http://www.splatalogue.net (F. J. Lovas, Remijan et al. 2007) queried through the Astroquery interface (Ginsburg et al. 2017). For NH_2D and ND_2H, the frequencies and constants are from the Cologne Database for Molecular Spectroscopy (Müller et al. 2005).

6.1 Lines in the 1–52 GHz frequency range

The VLA receivers operate mainly in eight different bands with a combined continuous spectral coverage between 1 and 50 GHz.[3] With a schedule of different configurations, it achieves resolutions ranging from 0.043 to 46 arcsec. ALMA band 1 covers the frequency range 35–52 GHz (50–52 GHz is on best effort basis). The typical 3σ sensitivity of an observation run of about 10 h for VLA is 1 mJy in a 0.4 arcsec beam, valid between around 4 and 48 GHz.[4] For ALMA band 1, it is not possible to estimate the sensitivity with the online estimator, but it is assumed to be at a similar level to VLA ($\sim$1 mJy/beam), but with less observation time. The resulting LTE spectra for NH_3, NH_2D, and ND_2H in the VLA spectral range (1–50 GHz) is shown in Fig. 7 . The main lines to target with VLA are between 15 and 38 GHz for NH_3, and while seven lines of NH_2D are available in the same range, there are no ND_2H lines predicted to be above the 3σ level. The NH_2D line at 49.96 GHz is just at the edge of the Q band where sensitivity is significantly lower. Furthermore, as optical depth might be an issue for some of the transitions, a wide spread in E_u and Einstein A coefficient is the best strategy. The beam is matched to the rough size of the warm inner regions of the sources, once abundances and emission extent has been determined more exact with high sensitivity observations, it is possible to observe the lines at higher spatial and spectral resolution to constrain the distribution and kinematic origin of ammonia further. As can be seen, only a few lines of deuterated ammonia are available with VLA, and they are spread out over several bands, which is not an ideal observing strategy. Furthermore, no ND_2H transitions can be detected with VLA, thus we have to turn to higher frequencies and observe the target with the ALMA telescope. ALMA band 1 covers a few NH_3 and NH_2D lines, and could thus be used for observations,

Figure 7. Synthetic spectrum of NH_3, NH_2D, and ND_2H in the VLA frequency range. The model assumes $T_{ex} = 200$ K, a source size of 0.4 arcsec, and a beam of 0.4 arcsec. Letters at top indicate the relevant VLA band, and where 'ALMA 1' indicates the region of ALMA band 1 (35–52 GHz). The solid and dashed line shows the 1 and 3σ levels, respectively.

Figure 8. Synthetic spectrum of NH_2D in the ALMA frequency range. The model assumes $T_{ex} = 200$ K, a source size of 0.4 arcsec and a beam of 0.4 arcsec. The numbers at the top indicate the relevant ALMA band. Note the change in scale of the flux around 20 mJy. The solid and dashed lines shows the 1 and 3σ levels, respectively.

once operational. However, the main transition bands are covered by VLA and is thus the most suitable instrument.

6.2 Lines 65–720 GHz frequency range

The ALMA telescope array is equipped with receivers covering frequencies between 35 and 720 GHz in bands 1 through 9. Band 1 and 2, i.e. 35–90 GHz is under construction, thus the band 2 sensitivity is assumed to be similar as in band 3 (and band 1 sensitivity similar to VLA at same frequency). With baselines ranging from 160 m to 16 km, the resulting spatial resolution range from 0.020 to 4.8 arcsec. The typical 3σ sensitivity of an observation run of about 4 h integration time in a 0.4 arcsec beam differs between the bands, but lies around 0.7 mJy beam^{-1} in bands 1 through 7, and increases to around 4 mJy beam^{-1} in band 8 and 5 mJy beam^{-1} in band 9. However, the high frequency bands (band 8 and 9) need lower levels

---

[3] This excludes band 4 and the P band, operating below 1 GHz, but with only on a limited number of antennas and at a highest angular resolution of $\sim$5.6 arcsec, which is not relevant for this study.

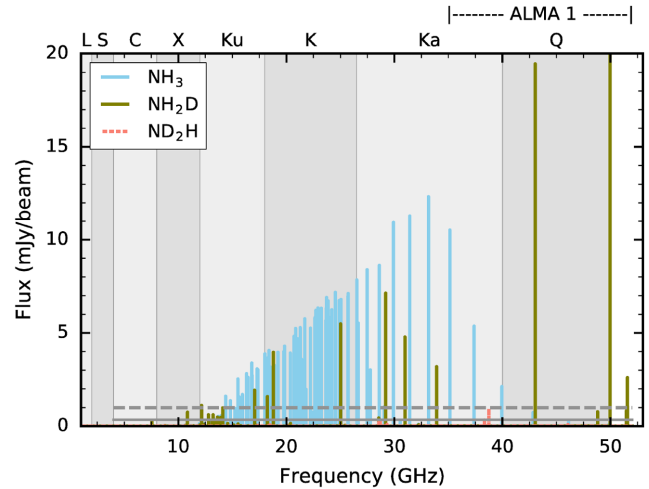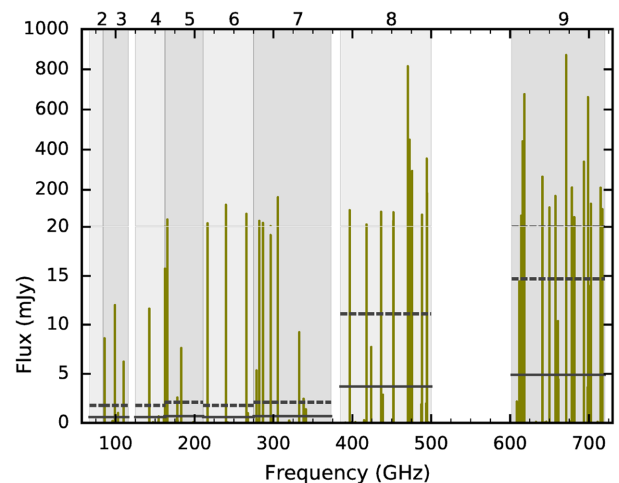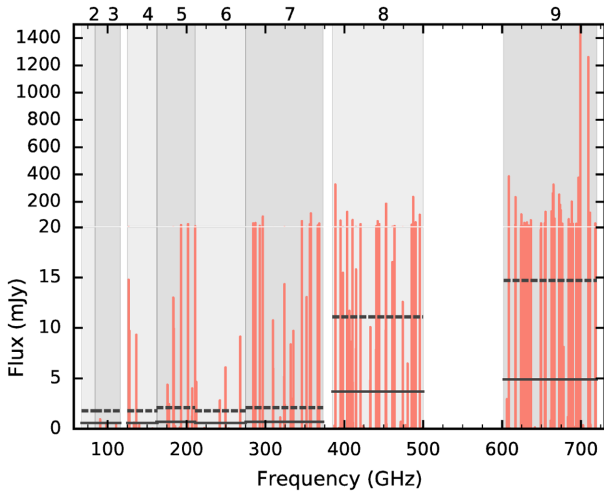[4] Assuming 27 antennas, winter conditions, 2.2 km s^{-1} channel width, and an elevation of the target between 50 and 90°.

Figure 9. Synthetic spectrum ND_2H in the ALMA frequency range. The model assumes $T_{ex} = 200$ K, a source size of 0.4 arcsec and a beam of 0.4 arcsec. The numbers at the top indicate the relevant ALMA band. Note the change in scale of the flux around 20 mJy. The solid and dashed lines shows the 1 and 3σ levels, respectively.

of precipitable water vapour for these sensitivities. Thus, they are less favourable since less time is available for such observations, and there are transitions at lower frequencies.

As Figs 8 and 9 show, there are several lines of NH_2D and ND_2H presented well above the sensitivity level in most receiver bands. However the highest overlapping density of lines with high signal-to-noise (SNR) ratio is in band 7. Thus, the best target for deuterated ammonia with ALMA is in band 7, around 300 GHz. The higher frequency bands, band 8 and 9, need better weather for a given sensitivity, and are as such less efficient to observe. Furthermore, given the high SNR of the lines in band 7, it is possible to observe sources with lower column densities.

While the main frequency region for NH_3 is in the VLA receiver bands, there are two lines in ALMA band 7 that might be possible to detect (at 354 and 361 GHz). However, their high energy levels ($E_u \approx 800$ K) and low Einstein A ($log_{10}(A_{ij}) \approx -8$) make them more difficult to detect. In addition to the target lines of NH_2D and ND_2H, there are two ND_3 lines as well: the ND_3 $1_{0,0} - 0_{0,1}$ transition at 307 GHz, and the $1_{0,1} - 0_{0,0}$ transition at 310 GHz. Thus, with a single spectral setup and around 4 h of ALMA integration time in band 7, it should be possible to characterize the NH_2D, ND_2H, and ND_3 column densities, all at once. This further highlights the importance of band 7 for ALMA observations of ammonia. Combining this with VLA observations of NH_3, it is possible to constrain the ratios studied here, and constrain the amount of N I in young, deeply embedded protostars. Once again, targeting a combination of transitions with different energy levels and transition probabilities is the best strategy to constrain the abundances.

7 CONCLUSION

Partitioning of elemental nitrogen in star-forming regions is not well constrained. Most nitrogen is expected to be partitioned among N I, N_2, and icy N-bearing molecules, such as NH_3 and N_2. Neither N I nor N_2 is directly observable in the cold gas, while the N_2 abundance can be constrained via a proxy molecule, N_2H^+. In this paper, we have proposed an indirect way to constrain the amount of atomic nitrogen in the cold gas of star-forming clouds, via deutera-

tion in ammonia ice. Using a simple analytical model and gas–ice astrochemical simulations, which trace the evolution from the formation of molecular clouds to protostellar cores, we showed that the evolution of the N I abundance in the cold (~ 10 K) ice formation stages is reflected in the icy $[ND_2H/NH_2D]/[NH_2D/NH_3]$ ratio. If N I remains as the primary reservoir of nitrogen during cold ice formation stages, the ratio is close to the statistical value of one-third and lower than unity, whereas if N I is largely converted into N-bearing molecules, the ratio should be larger than unity. The $[ND_2H/NH_2D]/[NH_2D/NH_3]$ ratio in ice mantles in star-forming clouds can be quantified with VLA and ALMA observations of the inner warm regions around protostars, where ammonia ice has completely sublimated, with reasonable integration times (Section 6).

We also found that partitioning of nitrogen between NH_3 ice and N_2 is sensitive to the photodesorption yield of NH_3 ice. The fraction of elemental nitrogen locked in NH_3 ice decreases with increasing the photodesorption yield of NH_3 ice, while that in N_2 increases. The increased efficiency of NH_3 photodesorption slows down the accumulation of NH_3 ice, while it assists the conversion of N I into N_2; photodesorbed NH_3 is further photodissociated in the gas phase and the photofragment, NH_2 or NH, reacts with N I to form N_2 (Section 4.2).

Finally, as demonstrated in this paper for nitrogen and in Furuya et al. (2016) for oxygen, multiple deuteration can be a strong tool to constrain the evolution of atomic reservoirs in the cold gas. The method could be applied to other elements, such as sulphur, by observing for example, H_2S, H_2CS, and their deuterated forms, if they are mainly formed by surface reactions. However, to do that, laboratory and theoretical studies of their formation and deuteration pathways on surfaces are necessary.

REFERENCES

Aikawa Y., 2013, Chem. Rev., 113, 8961
Aikawa Y., Herbst E., 1999, ApJ, 526, 314
Aikawa Y., Wakelam V., Hersant F., Garrod R., Herbst E., 2012, ApJ, 760, 40
Arasa C., Koning J., Kroes G.-J., Walsh C., van Dishoeck E. F., 2015, A&A, 575, 121
Bergin E. A., Tafalla M., 2007, ARA&A, 45, 339
Bergin E. A., Hartmann L. W., Raymond J. C., Ballesteros-Paredes J., 2004, ApJ, 612, 921
Bertin M. et al., 2012, Phys. Chem. Chem. Phys., 14, 9929
Bertin M. et al., 2013, ApJ, 779, 120
Bisschop S. E., Jørgensen J. K., Bourke T. L., Bottinelli S., van Dishoeck E. F., 2008, A&A, 488, 959
Boogert A. C. A., Ehrenfreund P., 2004, in Witt A. N., Clayton G. C., Draine B. T., eds, ASP Conf. Ser. Vol. 309, Astrophysics of Dust. Astron. Soc. Pac., San Francisco, p. 547
Boogert A. C. A., Blake G. A., Tielens A. G. G. M., 2002, ApJ, 577, 271
Boogert A. C. A., Gerakines P. A., Whittet D. C. B., 2015, ARA&A, 53, 541
Bottinelli S. et al., 2004, ApJ, 617, L69

Cazaux S., Caselli P., Spaans M., 2011, ApJ, 741, L34
Chang Q., Herbst E., 2014, ApJ, 787, 135
Chang Q., Cuppen H. M., Herbst E., 2007, A&A, 469, 973
Charnley S. B., Tielens A. G. G. M., Rodgers S. D., 1997, ApJ, 482, L203
Choi M., Tatematsu K., Park G., Kang M., 2007, ApJ, 667, L183
Choi M., Tatematsu K., Kang M., 2010, ApJ, 723, L34
Collings M. P., Anderson M. A., Chen R., Dever J. W., Viti S., Williams D. A., McCoustra M. R. S., 2004, MNRAS, 354, 1133
Coutens A. et al., 2012, A&A, 539, 132
Coutens A., Jørgensen J. K., Persson M. V., van Dishoeck E. F., Vastel C., Taquet V., 2014, ApJ, 792, L5
Coutens A. et al., 2016, A&A, 590, L6
Cuppen H. M., Herbst E., 2007, ApJ, 668, 294
Daranlot J., Hincelin U., Bergeat A., Costes M., Loison J. C., Wakelam V., Hickson K. M., 2012, PNAS, 109, 10233
Draine B. T., 1978, ApJS, 36, 595
Elsila J., Allamandola L. J., Sandford S. A., 1997, ApJ, 479, 818
Espinosa-Garcia J., Corchado J. C., 2010, J. Phys. Chem. A, 114, 4455
Fayolle E. C., Bertin M., Romanzin C., Michaut X., Öberg K. I., Linnartz H., Fillion J. H., 2011, ApJ, 739, L36
Fayolle E. C., Balfe J., Loomis R., Bergner J., Graninger D., Rajappan M., Öberg K. I., 2016, ApJ, 816, L28
Fedoseev G., Ioppolo S., Zhao D., Lamberts T., Linnartz H., 2015a, MNRAS, 446, 439
Fedoseev G., Ioppolo S., Linnartz H., 2015b, MNRAS, 446, 449
Fedoseev G., Chuang K.-J., van Dishoeck E. F., Ioppolo S., Linnartz H., 2016, MNRAS, 460, 4297
Furuya K., Aikawa Y., Hincelin U., Hassel G. E., Bergin E. A., Vasyunin A. I., Herbst E., 2015, A&A, 584, 124
Furuya K., van Dishoeck E. F., Aikawa Y., 2016, A&A, 586, 127
Garrod R. T., Herbst E., 2006, A&A, 457, 927
Garrod R. T., Pauly T., 2011, ApJ, 735, 15
Gibb E. L., Whittet D. C. B., Boogert A. C. A., Tielens A. G. G. M., 2004, ApJS, 151, 35
Ginsburg A. et al., 2017, Astrophysics Source Code Library, record ascl:1708.004
Goldsmith P. F., Langer W. D., 1999, ApJ, 517, 209
Harju J. et al., 2017, A&A, 600, 61
Hasegawa T. I., Herbst E., 1993, MNRAS, 263, 589
Hassel G. E., Herbst E., Bergin E. A., 2010, A&A, 515, 66
He J., Acharyya K., Vidali G., 2016, ApJ, 823, 56
Heays A. N., Bosman A. D., van Dishoeck E. F., 2017, A&A, 602, 105
Herbst E., Klemperer W., 1973, ApJ, 185, 505
Hidaka H., Watanabe M., Kouchi A., Watanabe N., 2009, ApJ, 702, 291
Hidaka H., Watanabe M., Kouchi A., Watanabe N., 2011, Phys. Chem. Chem. Phys., 13, 15798
Hily-Blant P., Walmsley M., Pineau des Forêts G., Flower D., 2010, A&A, 513, 41
Hirota T. et al., 2008, PASJ, 60, 37
Hugo E., Asvany O., Schlemmer S., 2009, J. Chem. Phys., 130, 164302
Jenkins E. B., 2009, ApJ, 700, 1299
Jørgensen J. K., Bourke T. L., Nguyen Luong Q., Takakuwa S., 2011, A&A, 534, A100
Jørgensen J. K. et al., 2016, A&A, 595, A117
Kalvāns J., Shmeld I., Kalnin J. R., Hocuk S., 2017, MNRAS, 467, 1763
Knauth D. C., Andersson B.-G., McCandliss S. R., Warren Moos H., 2004, Nature, 429, 636
Lamberts T., Cuppen H. M., Fedoseev G., Ioppolo S., Chuang K.-J., Linnartz H., 2014, ApJ, 570, 57
Le Gal R., Hily-Blant P., Faure A., Pineau des Forêts G., Rist C., Maret S., 2014, A&A, 562, 83
Li X., Heays A. N., Visser R., Ubachs W., Lewis B. R., Gibson S. T., van Dishoeck E. F., 2013, A&A, 555, A14
Linsky J. L., 2003, Space Sci. Rev., 106, 49
Lis D. C., Roueff E., Gerin M., Phillips T. G., Coudert L. H., van der Tak F. F. S., Schilke P., 2002, ApJ, 571, L55
Loinard L., Castets A., Ceccarelli C., Caux E., Tielens A. G. G. M., 2001, ApJ, 552, L163

Loinard L., Torres R. M., Mioduszewski A. J., Rodríguez L. F., 2008, ApJ, 675, L29
Loison J.-C., Wakelam V., Hickson K. M., 2014, MNRAS, 443, 398
Maret S., Bergin E. A., Lada C. J., 2006, Nature, 442, 425
Maret S., Faure A., Scifoni E., Wiesenfeld L., 2009, MNRAS, 399, 425
Martin-Domenech R., Cruz-Diaz G. A., Munoz Caro G. M., 2017, MNRAS, 473, 2575
Masunaga H., Inutsuka S., 2000, ApJ, 531, 350
McGonagle D., Irvine W. M., Minh Y. C., Ziurys L. M., 1990, ApJ, 359, 121
Minissale M., Congiu E., Dulieu F., 2016, A&A, 585, 146
Müller H. S. P., Schlöder F., Stutzki J., Winnewisser G., 2005, J. Mol. Struct., 742, 215
Murakawa K., Tamura M., Nagata T., 2000, ApJS, 128, 603
Noble J. A., Congiu E., Dulieu F., Fraser H. J., 2012, MNRAS, 421, 768
Oba Y., Watanabe N., Hama T., Kuwahata K., Hidaka H., Kouchi A., 2012, ApJ, 749, 67
Öberg K. I., van Broekhuizen F., Fraser H. J., Bisschop S. E., van Dishoeck E. F., Schlemmer S., 2005, ApJ, 621, L33
Öberg K. I., Boogert A. C. A., Pontoppidan K. M., van den Broek S., van Dishoeck E. F., Bottinelli S., Blake G. A., Evans N. J., 2011, ApJ, 740, 109
Pagani L., Bourgoin A., Lique F., 2012, A&A, 548, L4
Parise B., Ceccarelli C., Tielens A. G. G. M., Castets A., Caux E., Lefloch B., Maret S., 2006, A&A, 453, 949
Pauly T., Garrod R. T., 2016, ApJ, 817, 146
Persson M. V., Jørgensen J. K., van Dishoeck E. F., 2013, A&A, 549, L3
Persson M. V., Jørgensen J. K., van Dishoeck E., Harsono D., 2014, ApJ, 563, 74
Persson M. V., Harsono D., Tobin J. J., van Dishoeck E. F., Jørgensen J. K., Murillo N., Lai S.-P., 2016, A&A, 590, A33
Pontoppidan K. M., 2006, A&A, 453, L47
Pontoppidan K. M., van Dishoeck E. F., Dartois E., 2004, A&A, 426, 925
Przybilla N., Nieva M.-F., Butler K., 2008, ApJ, 688, L103
Remijan, A. J., Markwick-Kemper, A., & ALMA Working Group on Spectral Line Frequencies, 2007, Bull. Am. Astron. Soc., 39, 132 .11
Rodgers S. D., Charnley S. B., 2002, Planet. Space Sci., 50, 1125
Rodgers S. D., Charnley S. B., 2008, MNRAS, 385, L48
Rodgers S. D., Millar T. J., 1996, MNRAS, 280, 1046
Roueff E., Lis D. C., van der Tak F. F. S., Gerin M., Goldsmith P. F., 2005, A&A, 438, 585
Roueff E., Loison J. C., Hickson K. M., 2015, A&A, 576, A99
Schwarz K. R., Bergin E. A., 2014, 797, 113
Sewilo M., Wiseman J., Indebetouw R., Charnley S. B., Pineda J. E., Lindberg J. E., Qin S.-L., 2017, ApJ, 849, 68
Shah R. Y., Wootten A., 2001, ApJ, 554, 933
Sipilä O., Caselli P., Harju J., 2013, A&A, 554, A92
Taquet V., Ceccarelli C., Kahane C., 2012, ApJ, 748, L3
Taquet V., Charnley S. B., Sipilä O., 2014, ApJ, 791, 1
Tielens A. G. G. M., Hagen W., 1982, A&A, 114, 245
Vasyunin A. I., Herbst E., 2013, ApJ, 762, 86
Viala Y. P., 1986, A&AS, 64, 391
Villanueva G. L., Mumma M. J., Bonev B. P., Di Santi M. A., Gibb E. L., Böhnhardt H., Lippi M., 2009, ApJ, 690, L5
Visser R., van Dishoeck E. F., Black J. H., 2009, A&A, 503, 323
Wakelam V., Smith I. W. M., Loison J.-C., Talbi D., Klippenstein S. J., Bergeat A., Geppert W. D., Hickson K. M., 2013, preprint (arXiv:1310.4350)
Wakelam V., Loison J. C., Mereau R., Ruaud M., 2017, Mol. Astrophys., 6, 22
Whittet D. C. B., 1993, Dust and Chemistry in Astronomy. Institute of Physics Publishing, Bristol and Philadelphia, p. 9
Wilson T. L., 1999, Rep. Prog. Phys., 62, 143
Wilson T. L., Rood R., 1994, ARA&A, 32, 191
Womack M., Ziurys L. M., Wyckoff S., 1992, ApJ, 393, 188

This paper has been typeset from a TeX/LaTeX file prepared by the author.